# Effect of Widmanstätten η phase on tensile shear strength of resistance spot welding joints of A286 superalloy

Óscar Martín[a,*], Pilar De Tiedra[b], Manuel San-Juan[c]

[a] Ingeniería de los Procesos de Fabricación, Departamento CMeIM/EGI/ICGF/IM/IPF, Universidad de Valladolid, Escuela de Ingenierías Industriales, Paseo del Cauce 59, Valladolid 47011, Spain.

[b] Ciencia de los Materiales e Ingeniería Metalúrgica, Departamento CMeIM/EGI/ICGF/IM/IPF, Universidad de Valladolid, Escuela de Ingenierías Industriales, Paseo del Cauce 59, Valladolid 47011, Spain. E-mail: tiedra@eii.uva.es.

[c] Ingeniería de los Procesos de Fabricación, Departamento CMeIM/EGI/ICGF/IM/IPF, Universidad de Valladolid, Escuela de Ingenierías Industriales, Paseo del Cauce 59, Valladolid 47011, Spain. E-mail: mansan@eii.uva.es.

* Corresponding author. Ph.: +34-983185037, Fax: +34-983423310, E-mail: oml@eii.uva.es (Ó. Martín)

## *Abstract*

This work aims to study the effect of Widmanstätten η phase on tensile shear strength (TSS) of resistance spot welding joints (RSW) of A286 superalloy subjected to post-weld high temperature aging treatment. The tensile shear test specimens were welded in the solution treated condition, and then subjected to six different post-weld aging treatments (at an aging temperature of 840 °C for six different aging times). The as-cast dendritic microstructure of the weld nugget and the austenite equiaxed-grain microstructure of the base metal have a different response to the post-weld high temperature aging treatment. Growth of Widmanstätten η phase in the weld nugget is faster than in the base metal. While in the base metal the Widmanstätten η phase precipitates into the grain, in the weld nugget precipitates at the interdendritic region because of the segregation of Ti towards the last-to-solidify interdendritic regions (studied by performing SEM/EDX analysis). Although the hardness increases with the presence of Widmanstätten η phase, the increase in hardness does not necessarily imply an increase in the experimental TSS.

*Keywords:* Resistance spot welding; A286 superalloy; Post-weld aging treatment; Widmanstätten η phase; γ' precipitates

# 1 Introduction

Precipitation-strengthened A286 austenitic stainless steel is an iron-nickel based alloy that is extensively used in gas turbine jet engines, superchargers and hydrogen service due to its high strength, acceptable hydrogen performance and excellent corrosion resistance [1].

A286 superalloy is strengthened by the precipitation of the ordered fcc γ' phase ($Ni_3(Al,Ti)$), coherent with the austenite matrix [2–4]. The γ' phase is unstable and, after a sufficiently long aging treatment at sufficiently high temperature, dissolves to form the stable hcp η phase ($Ni_3Ti$) [4–7]. The η phase may precipitate at grain boundary by cellular reaction at lower aging temperatures, or into the grain with Widmanstätten morphology at higher aging temperatures [7–9]. This phenomenon, as explained by Seifollahi et al. [7] and by Asgari [8] considering a diffusive mechanism for growth of the hcp η precipitates in the fcc matrix, occurs in such a way that at lower temperatures the matrix diffusion is slower than the grain boundary diffusion and, hence, cellular η grows much faster than Widmanstätten η, whilst at higher temperatures matrix diffusion is accelerated and the Widmanstätten morphology dominates. While the cellular η phase precipitation at grain boundary may be detrimental to the mechanical properties [10–14], the Widmanstätten η phase precipitation into the grain which may increase strength of the alloy at the expense of its ductility [8].

A286 superalloy is a difficult material to weld due to its high susceptibility to hot cracking in the fusion zone [15]. Solidification cracking occurs during the last stages of solidification because of the inability of the nearly solidified weld metal to accommodate shrinkage stresses [16], and it is associated with the segregation of titanium and other solutes towards the last-to-solidify interdendritic regions that promotes the formation of a low melting point γ/Laves eutectic [16–21].

The general practice in welding superalloys is to employ a weaker, more ductile austenitic filler metal than the base metal to minimize weld cracking but, when the maximum joint strength is required, filler metal of base metal composition is recommended [22]. Thus, resistance spot welding (RSW), which is an autogenous welding process and is widely used for joining sheet steel in the automotive industry [23], can be an interesting method for welding A286 superalloy sheets [24].

The aim of the present work is to study the effect of Widmanstätten η phase, which precipitates after a post-weld high temperature aging treatment (to which as-cast dendritic microstructure of the weld nugget and austenite equiaxed-grain microstructure of the base metal have different response), on tensile shear strength (TSS) of RSW joints of A286 superalloy.

# 2 Experimental Procedure

## 2.1 Materials

The chemical composition of the A286 superalloy sheets welded by RSW is shown in Table 1. The sheet thickness was 1 mm.

**Table 1.** Chemical composition of A286 superalloy sheets (wt %).

| C | Si | Mn | P | S | Cr | Mo | Ni | V | Ti | Al | B | Fe |
|---|---|---|---|---|---|---|---|---|---|---|---|---|
| 0.032 | 0.50 | 1.24 | 0.011 | <0.0003 | 14.98 | 1.18 | 24.74 | 0.29 | 2.30 | 0.16 | 0.0046 | Bal. |

The tensile shear test specimens were welded in the solution treated condition [22], and then subjected to six different post-weld aging treatments (see Table 2). This solution treatment allows to: (i) reduce or even remove the effects of the mechanical history of the material [25]; and (ii) remove any possible chemical segregation associated with the formation of γ' and η phases because, as pointed out by Ratna and Sarma [26], the solvus temperature of γ' phase in A286 superalloy is 855 °C and, as demonstrated by Seifollahi et al. [7], the η phase is completely dissolved at 900 °C and the microstructure of A286 superalloy is free of η. According to Table 2, there were seven different tensile shear test specimens.

**Table 2.** Tensile shear test specimens. Specimen No. 0 was subjected to no aging treatment, i.e. it was in the solution treated condition. Each of different aging treatments was followed by air cooling.

| Solution treated condition | | RSW process | Aging treatment | | Specimen No. |
|---|---|---|---|---|---|
| Temperature (°C) | Time (h) | | Temperature (°C) | Time (h) | |
| 927 | 0.25 | WT = 0.36 s<br>WC = 6 kA<br>EF = 2300 N | N/A | N/A | 0 |
| | | | 840 | 0.5 | 1 |
| | | | | 10 | 2 |
| | | | | 25 | 3 |
| | | | | 50 | 4 |
| | | | | 100 | 5 |
| | | | | 200 | 6 |

The A286 superalloy sheets were welded with a single-phase alternating current (AC) 50 Hz equipment by using water-cooled truncated cone RWMA Group A Class 2 electrodes [27], with 16 mm body diameter and 5 mm face diameter. The controlled parameters in the RSW process

of the tensile shear test specimens were [28,29]: welding time (WT), welding current (WC), and electrode force (EF). The values of the welding parameters were fixed at WT = 0.36 s, WC = 6 kA and EF = 2300 N [17,24]; these values were chosen in order to maximize the weld nugget size, which increases with increasing heat input, and to minimize the effect of the expulsion phenomena, which is associated with an excessive heat input [30].

## 2.2 Scanning Electron Microscopy (SEM)

SEM was used to study the presence of γ' and η phases in the microstructure and to perform fractography analysis. SEM micrographs of the microstructure were obtained after mechanical polishing and electrolytic etching with etchant No. 83 according to ASTM E407-07e1 (at 6 V for 60 s in a solution of 10 g $CrO_3$ in 100 ml water) [31]. The SEM macrograph and the SEM micrograph for fractography analysis did not require metallographic preparation. SEM observations were conducted on a FEI-Quanta 200FEG operating at 20 kV and equipped with an energy dispersive X-ray analysis (EDX) to determine the chemical composition of interdendritic region.

## 2.3 Tensile shear testing

Tensile shear tests were carried out, on a Shimadzu UH-F500 kNA universal testing machine, at a crosshead speed of 2 mm/min [24,32,33], which, as explained by Marashi et al. [34], allows to consider the test as static. The tensile shear test specimens were prepared according to ISO 14273 [35]. Considering the possibility that the solution treatment does not completely remove the anisotropy of the material, it is mentioned that the loading direction of the tensile shear test is parallel to the rolling direction of the sheet material.

## 3 Results and discussion

The most important factor affecting TSS is the size of weld nugget [36,37], which is the weld metal of the RSW joint and is formed from the solidification of the molten metal after a heating by Joule effect [38] and hence has an as-cast dendritic microstructure (Fig.1).

The experimental TSS, which was obtained in the tensile shear test (Fig. 2), and the predicted TSS, which was used as a reference, of each of the seven tensile shear test specimens are shown in Fig. 3. The predicted TSS was obtained from Eq. (1) [39,40]:

$$P = 10^{-3} \cdot f \cdot t \cdot d \cdot \sigma_R \quad (1)$$

where $P$ is the predicted TSS (kN); $f$ is a coefficient whose value, given the results obtained by Martín et al. [24], was taken as 2.65, a value that is also consistent with those proposed by Sawhill and Baker [40] and by Radakovic and Tumuluru [41] for pullout failure mode, which,

as will be seen later, is the failure mode shown by all the tensile shear test specimens; $t$ is the sheet thickness (1 mm); $d$ is the weld nugget diameter whose value was taken as 5.5 mm; and $\sigma_R$ is the tensile strength (MPa) of the base metal, obtained in a tensile test conducted according to ISO 6892-1 [42], which is shown in Table 3. Although it must be mentioned that the tensile shear test is a fracture test on a specimen with a complex and notched geometry while the tensile test is a fracture test on a specimen with a smooth geometry, the predicted TSS obtained from Eq. (1) is appropriate to compare the different response to post-weld high temperature aging treatment of weld nugget and base metal although it simulates the behaviour of a "non-real" tensile shear test specimen where the weld nugget has the austenite equiaxed-grain microstructure of the base metal.

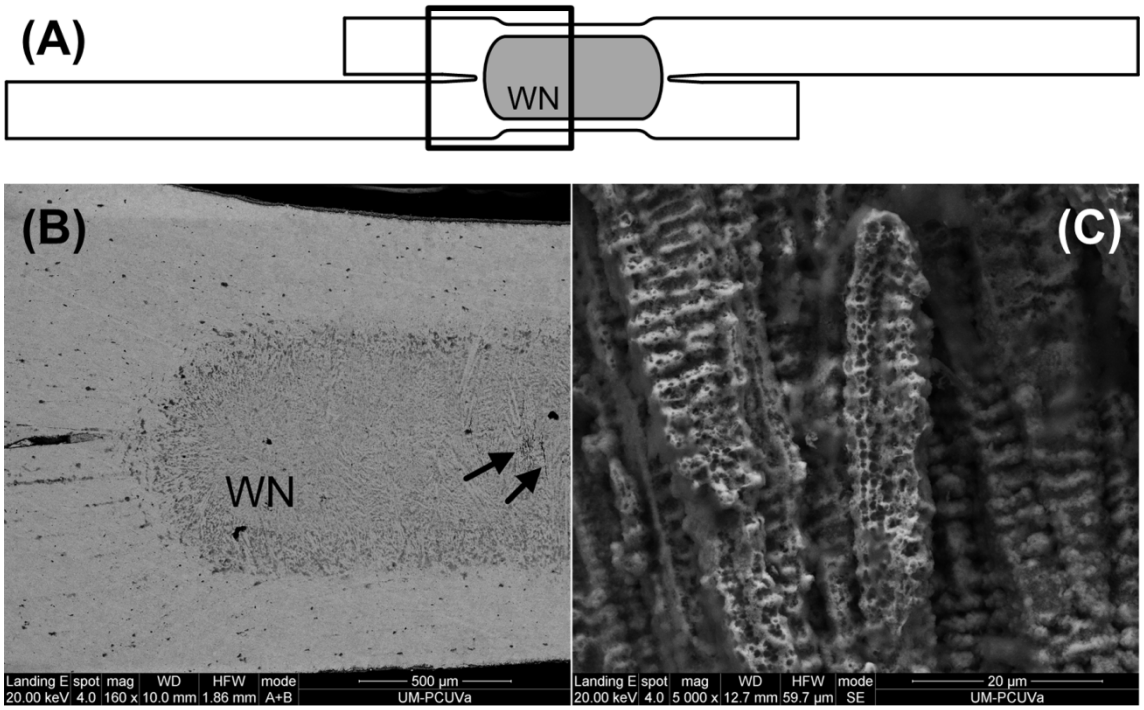


**Fig. 1.** (A) Diagram (not to scale) that shows the location of the area where the micrograph (B) was taken from the tensile shear test specimen; (B) SEM micrograph of a cross sectioned tensile shear test specimen (not mechanically tested) where the arrows show solidification cracks in the weld nugget (WN); (C) SEM micrograph of the as-cast dendritic microstructure of the weld nugget. Electrolytic etching with etchant No. 83 according to ASTM E407-07 [31].

**Table 3.** Tensile test specimens (without welding). The specimen subjected to no aging treatment, was in the solution treated condition. Each of different aging treatments was followed by air cooling. The tensile strength ($\sigma_R$), obtained in the tensile test, is that of the base metal of the tensile shear test specimens indicated in Table 2.

| Solution treated condition | | Aging treatment | | $\sigma_R$ (MPa) |
|---|---|---|---|---|
| Temperature (°C) | Time (h) | Temperature (°C) | Time (h) | |
| 927 | 0.25 | N/A | N/A | 592 |
| | | 840 | 0.5 | 756 |
| | | | 10 | 658 |
| | | | 25 | 696 |
| | | | 50 | 656 |
| | | | 100 | 650 |
| | | | 200 | 645 |

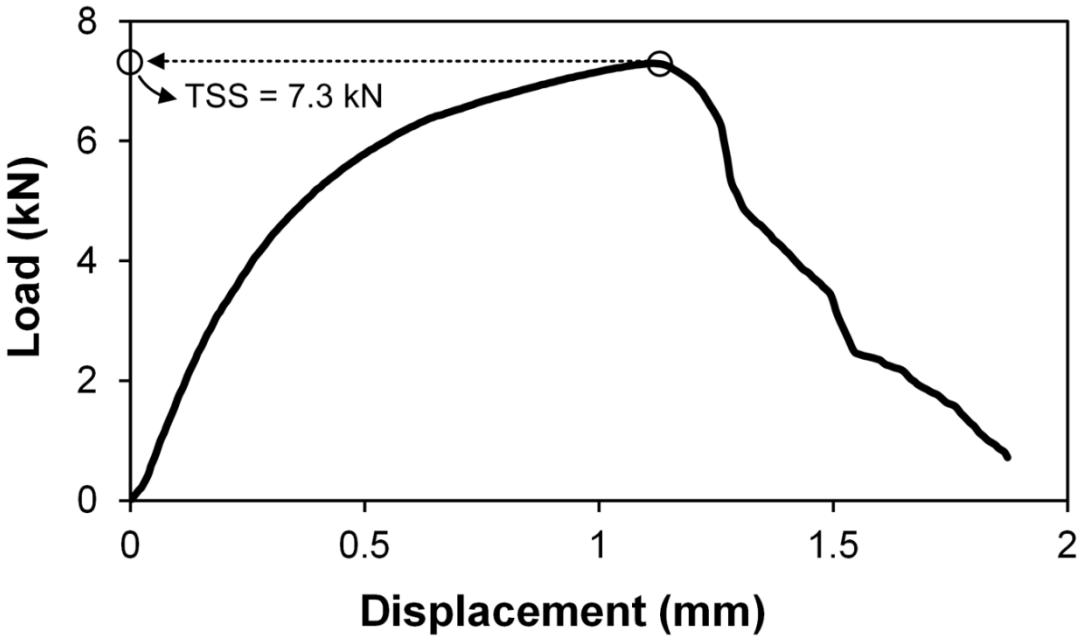


**Fig. 2.** Load vs. displacement curve obtained from the tensile shear test performed on specimen No. 4. The TSS is shown on the curve.

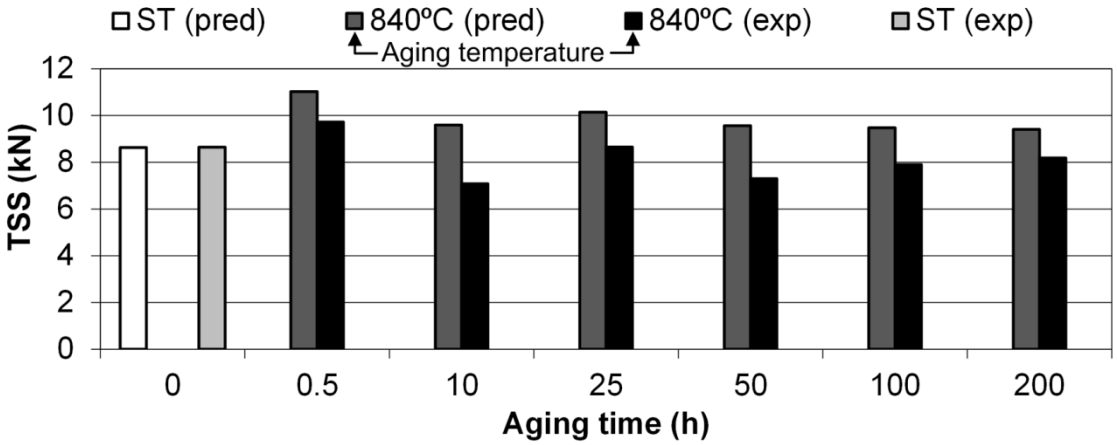


**Fig. 3.** Experimental (exp) TSS, which was obtained in the tensile shear test, and predicted (pred) TSS [39,40], of each of the seven tensile shear test specimens subjected to post-weld aging treatment. Specimen No. 0 was subjected to no post-weld aging treatment, i.e. it was in the solution treated (ST) condition and its aging time was considered as 0 h.

**Table 4.** The predicted TSS values obtained from Eq. (1) and the experimental TSS values of the tensile shear test specimens indicated in Table 2 are shown.

| Specimen No. | Predicted TSS (kN) | Experimental TSS (kN) |
|---|---|---|
| 0 | 8.63 | 8.65 |
| 1 | 11.02 | 9.72 |
| 2 | 9.59 | 7.08 |
| 3 | 10.14 | 8.65 |
| 4 | 9.56 | 7.30 |
| 5 | 9.47 | 7.9 |
| 6 | 9.41 | 8.18 |

As can be observed in Fig. 3 and in Table 4, the experimental and predicted values of TSS coincide for the specimens that were subjected to no post-weld aging treatment but, for the specimens that were subjected to post-weld aging treatment, the value of the experimental TSS is lower than that of the predicted TSS; this result shows that the as-cast dendritic microstructure of the weld nugget and the austenite equiaxed-grain microstructure of the base metal have a different response to the post-weld high temperature aging treatment. It is also noteworthy that, from an aging time of 10 h, the experimental values of TSS are even lower than that of the specimen that was subjected to no post-weld aging treatment.

The segregation of certain solute elements towards the last-to-solidify interdendritic regions of the weld nugget microstructure [17,18,21] (also studied in the solidification not related to welding processes [43,44]), was determined by performing SEM/EDX analysis on the interdendritic regions of the weld nugget of tensile shear test specimens No. 1 (Figs. 4 and 5 and Table 5).

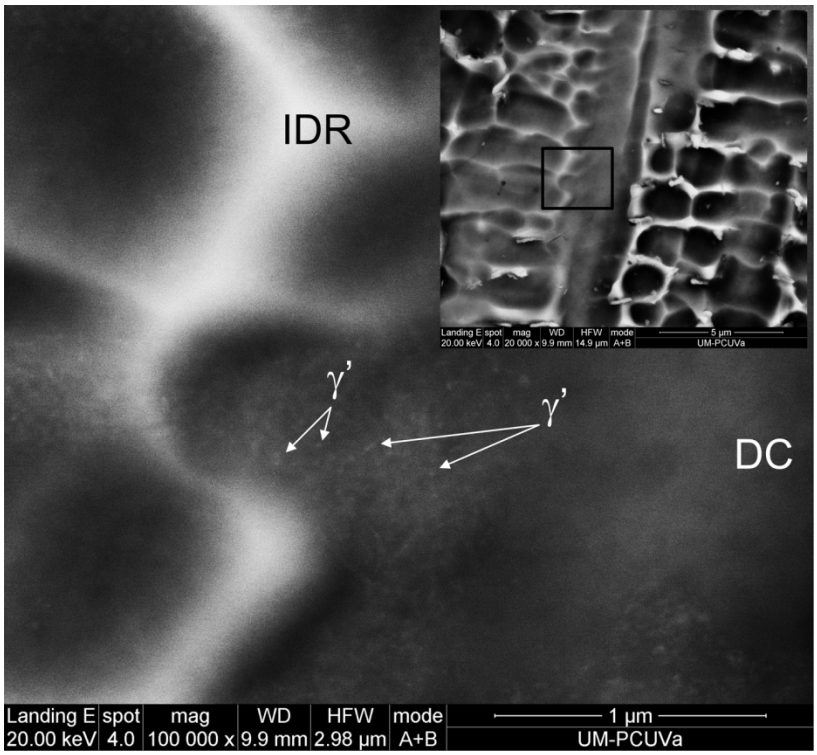


**Fig. 4.** SEM micrograph of the weld nugget of the tensile shear test specimen No. 1. The γ' precipitates are located adjacent to the interdendritic region (IDR) whilst, as can be seen, there are γ' depleted zones in the dendrite core (DC). The inset provides the location of the studied zone. Electrolytic etching with etchant No. 83 according to ASTM E407-07 [31].

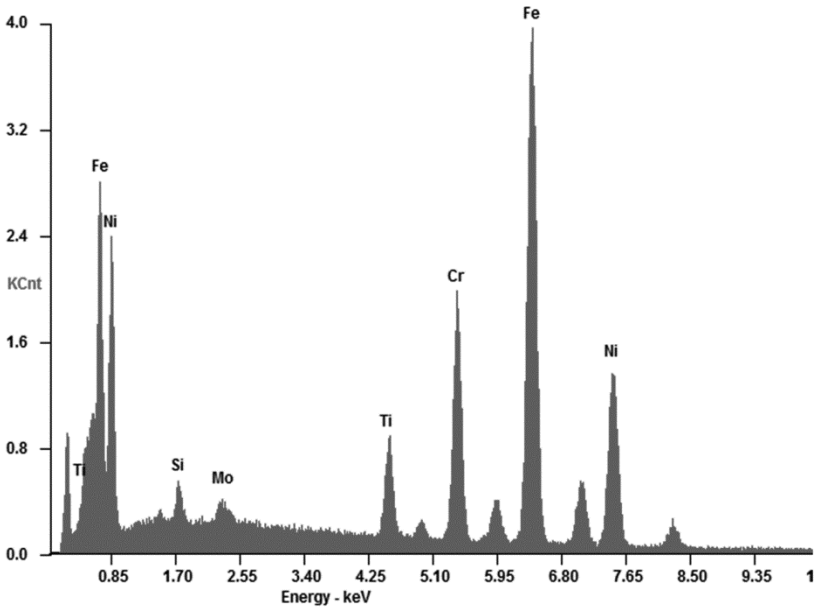


**Fig. 5.** EDX spectrum obtained from the interdendritic region of the weld nugget of specimen No. 1.

As shown in Table 5, the interdendritic region of the weld nugget is enriched, according to the ratio *k* between the interdendritic region composition and the nominal composition of the alloy [15], in Ti, Si, Ni and Mo and depleted in Fe and Cr [18]. These results are significant given that: (i) the higher the cooling rate of the welding process, the lower the segregation [45]; and (ii) the cooling rates associated with resistance spot welding are extremely rapid, on the order of $10^3$ to $10^5$ °C/s [46].

**Table 5.** Chemical composition (wt%) of interdendritic region of the weld nugget of specimen No. 1, determined by EDX and ratio k.

| Element | wt% | k |
|---|---|---|
| Si | 1.4 | 2.8 |
| Mo | 1.9 | 1.61 |
| Ti | 4.6 | 2 |
| Cr | 14.5 | 0.97 |
| Fe | 50 | 0.92 |
| Ni | 27.6 | 1.12 |

The most significant effect of this segregation in the weld nugget is the influence of the impoverishment in Ti of the dendrite core (which corresponds to the enrichment in Ti of the interdendritic regions) on the formation of two important Ti-rich phases: (i) the strengthening γ' phase; (ii) the Widmanstätten η phase (as will be seen later, after a post-weld aging treatment at an aging temperature of 840 °C, no cellular η phase forms in the weld nugget).

The segregation of Ti towards the interdendritic regions of the weld nugget gives rise to an heterogeneous distribution of γ' phase [1], which is associated with the development of γ' depleted zones in the dendrite core (Fig. 4), and which corresponds to a decrease in mechanical properties with respect to the base metal (Fig. 3) [15,24]. On the other hand, and as pointed out by Yan et al. [47], the growth of γ' precipitates in the weld metal, where the diffusivity of γ' forming elements is higher than in the base metal due to the higher concentration of vacancies, is faster than in the base metal; this result is consistent with the fact that, while in the weld nugget of specimen No. 1 (aging time of 0.5 h) the γ' precipitates are distinguishable (Fig. 4), in the base metal of the same specimen the γ' precipitates are not yet visible (Fig. 6).

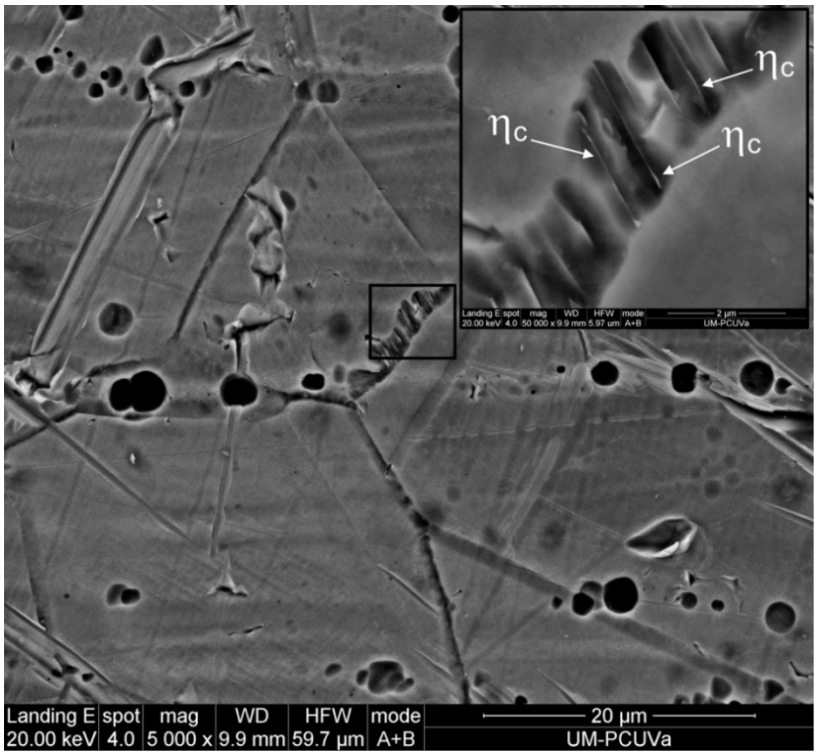


**Fig. 6.** SEM micrograph of the base metal of the tensile shear test specimen No. 1. The inset shows cellular η ($\eta_c$) phase at grain boundary. The γ' precipitates are not yet visible. Electrolytic etching with etchant No. 83 according to ASTM E407-07 [31].

The important decrease in the experimental TSS that occurs from an aging time of 10 h may be explained by the fact that, at an aging temperature of 840 °C, 10 h is the aging time from which there is evidence of the presence of Widmanstätten η phase. The decrease in the experimental TSS is favoured by the fact that Widmanstätten η phase forms at the expense of strengthening γ' phase [7,48], whose presence in the weld nugget decreases by increasing the aging time from 0.5h (Fig. 4) to 10h (Fig. 7). As a consequence of the different response to post-weld high temperature aging treatment of the weld nugget and the base metal, the Widmanstätten η plates are smaller but much more numerous in the weld nugget than in the base metal (Figs. 7-10). As can be observed, while in the base metal the Widmanstätten η phase, according to the literature, precipitates into the grain (Fig. 8), in the weld nugget precipitates at the interdendritic region (Fig. 7) because of the segregation of Ti towards the last-to-solidify interdendritic regions, which is a novel result of the present study.

The presence of Widmanstätten η phase increases with aging time and, since it forms at the expense of γ' phase, the presence of γ' phase decreases. This phenomenon leads, for an aging time of 50 h, to a drastic decrease in the presence of γ' precipitates (in the weld nugget there is no evidence of γ' precipitates (Fig. 9), and in the base metal its presence is limited (Fig. 10)).

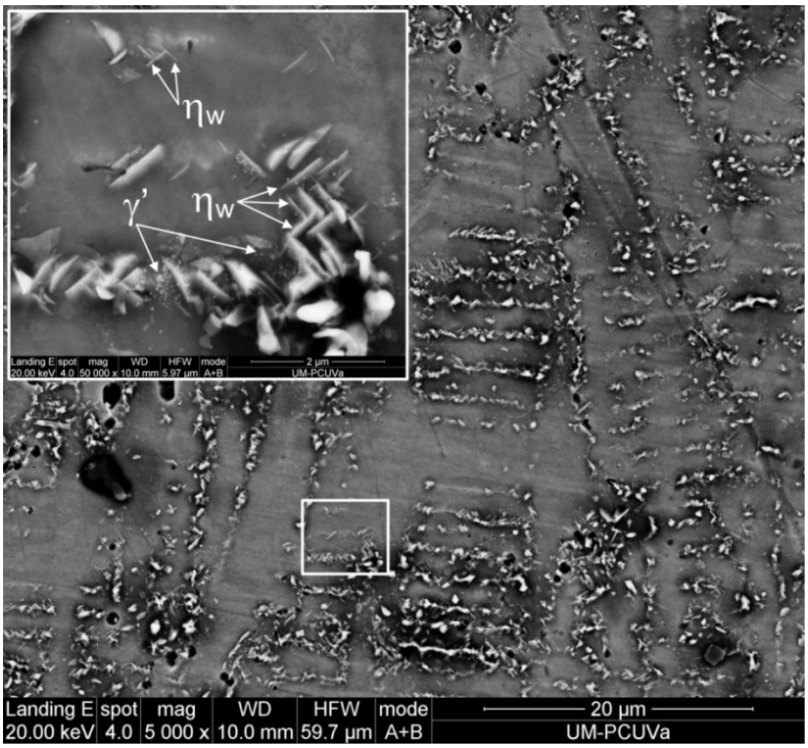


**Fig. 7.** SEM micrograph of the weld nugget of the tensile shear test specimen No. 2. The inset shows γ' precipitates and Widmanstätten η ($\eta_w$) phase located at the interdendritic region. The development of Widmanstätten η plates takes place along certain crystallographic directions [8]. Electrolytic etching with etchant No. 83 according to ASTM E407-07 [31].

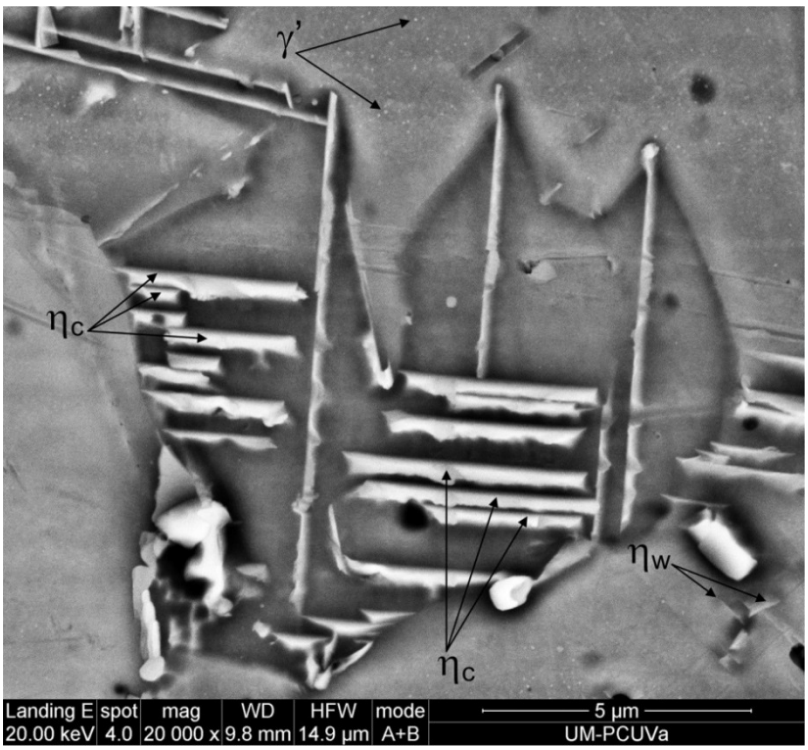


**Fig. 8.** SEM micrograph of the base metal of the tensile shear test specimen No. 2. The γ' precipitates are already visible, the Widmanstätten η ($\eta_w$) phase is formed into the grain and the cellular η ($\eta_c$) phase is also indicated. Electrolytic etching with etchant No. 83 according to ASTM E407-07 [31].

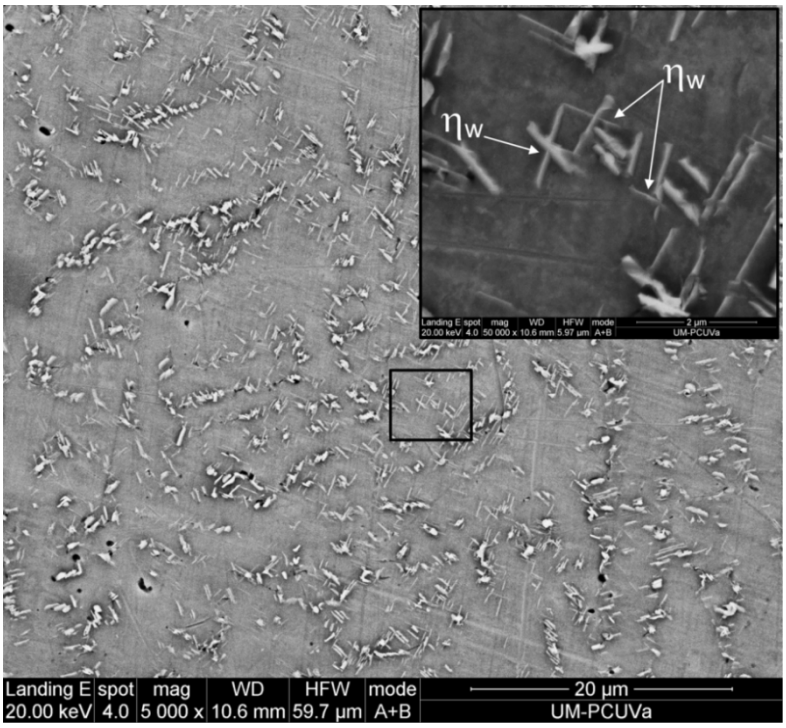


**Fig. 9.** SEM micrograph of the weld nugget of the tensile shear test specimen No. 4 where there is no evidence of the presence of γ' precipitates. The inset shows Widmanstätten η ($\eta_w$) phase located at the interdendritic region. Electrolytic etching with etchant No. 83 according to ASTM E407-07 [31].

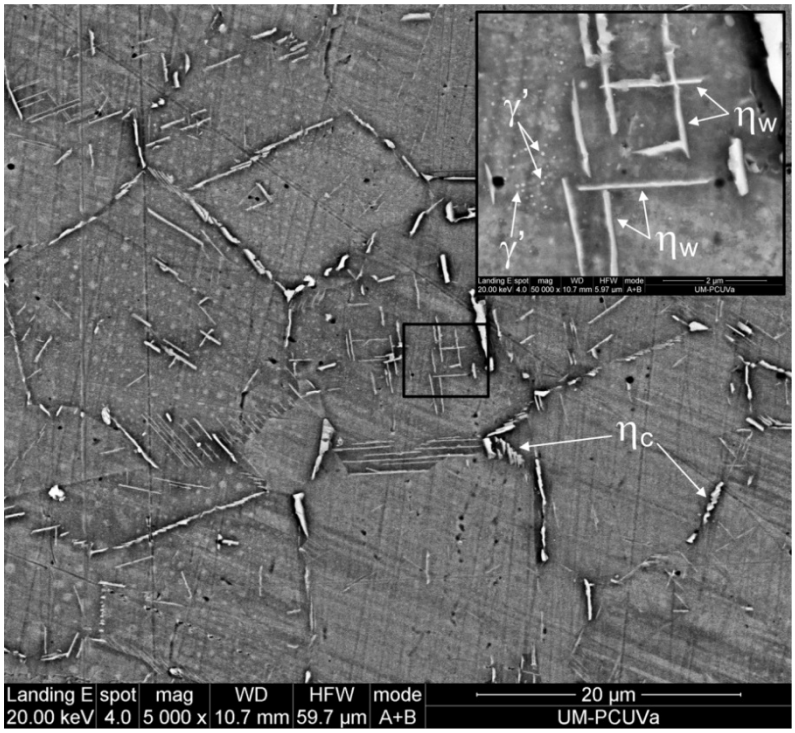


**Fig. 10.** SEM micrograph of the base metal of the tensile shear test specimen No. 4. The presence of Widmanstätten η ($\eta_w$), which is heterogeneously distributed into the grains, is lower than in the weld nugget (where is homogeneously distributed along the interdendritic regions, see Fig. 9). There is cellular η ($\eta_c$) phase at grain boundary. The inset shows γ' precipitates and $\eta_w$ phase into the grain. Electrolytic etching with etchant No. 83 according to ASTM E407-07 [31].

The relationship between the experimental TSS and the Widmanstätten η phase is highly complex because: (i) Widmanstätten η phase forms at the expense of strengthening γ' phase; (ii) the effect of γ' phase on mechanical behaviour is, in turn, complex because affects not only the strength but also the fracture toughness and, thus, the γ' size and morphology associated with higher yield strength also cause lower fracture toughness [49]; and (iii) although the hardness increases with the presence of Widmanstätten η phase (see Fig. 11, which shows a microhardness profile in the specimen No. 4 (for an aging time of 50 h) where the presence of Widmanstätten η phase in the weld nugget (Fig. 9) is greater than in the base metal (Fig. 10)), the increase in hardness does not necessarily imply an increase in experimental TSS, and this fact may be attributed to the hypothesis that the presence of Widmanstätten η phase causes brittleness; this hypothesis is compatible with the appearance of the fracture of all the tensile shear test specimens, which show a pullout failure mode (Figs. 12 and 13), and with the fractography analysis (Fig. 14), but, since the brittle fracture is only limited to the cleavage steps shown in Fig. 14, the lower experimental TSS should be attributed to other additional causes such as the lower hardness of the zone around the weld nugget (which is also consistent with the pullout failure mode of the tensile shear test specimens) and the presence in the weld nugget of solidification cracks (Fig. 1) that, as aforementioned, occur during the last stages of solidification because of the inability of the nearly solidified weld metal to accommodate shrinkage stresses [16], and that are associated with the segregation of titanium and other solutes towards the last-to-solidify interdendritic regions that promotes the formation of a low melting point γ/Laves eutectic [16–21].

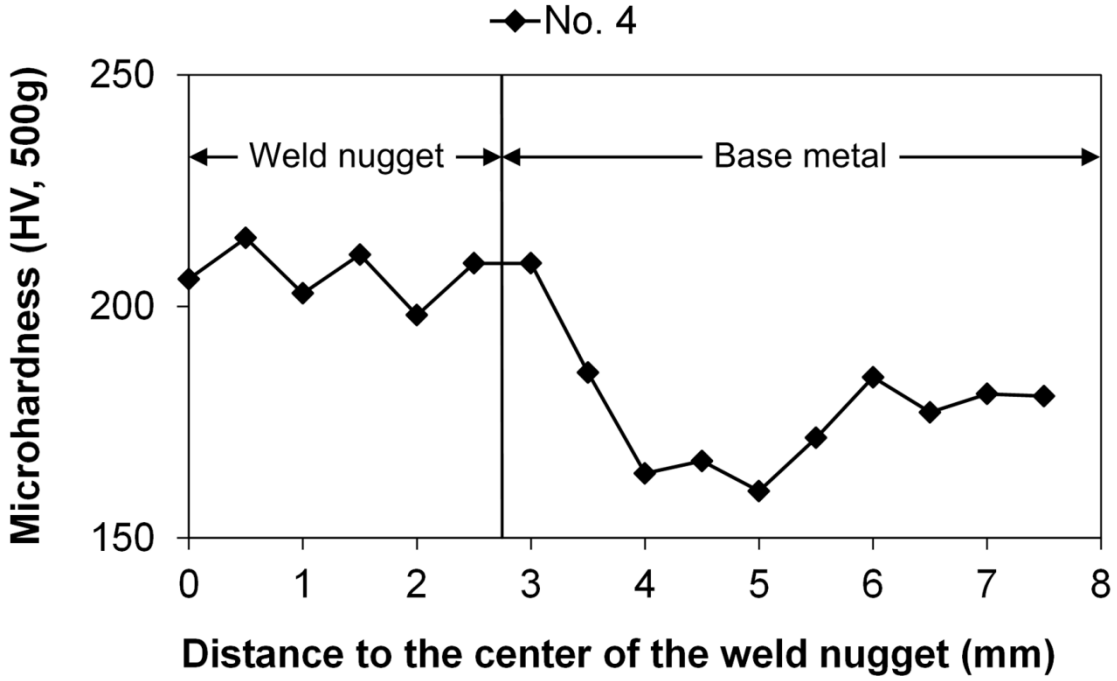


**Fig. 11.** Vickers microhardness profile in the cross sectioned tensile shear test specimen No. 4. The aging treatment does not eliminate the heat affected zone, which is present as a very narrow zone around the weld nugget [50].

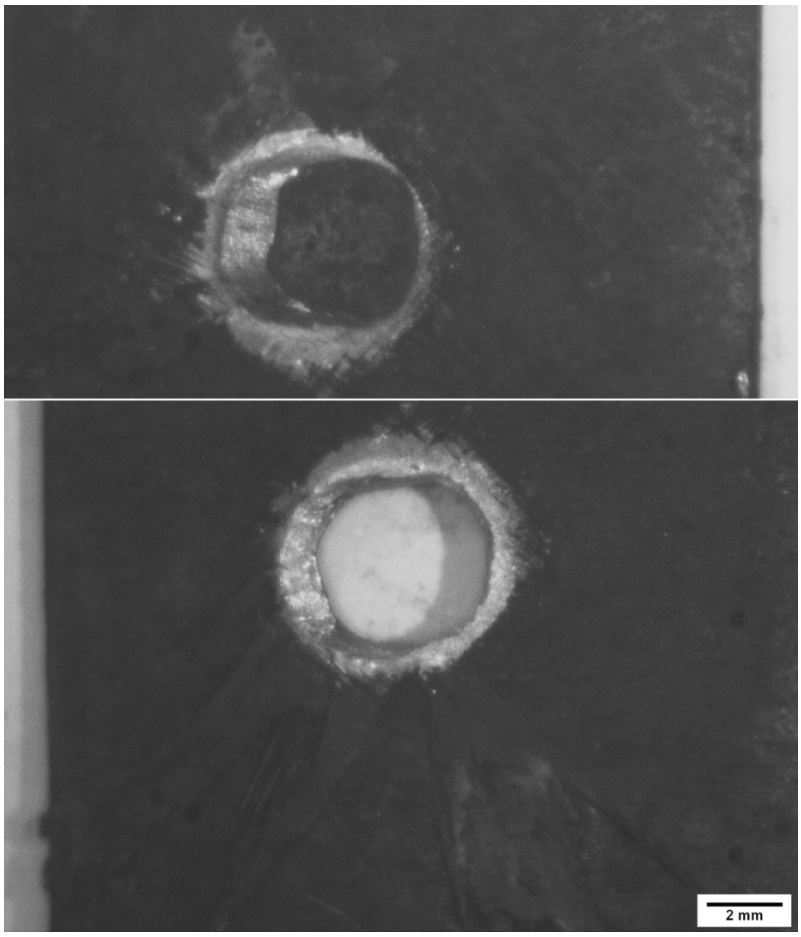


**Fig. 12.** Optical macrograph that shows pullout failure mode and expulsion phenomena in the tensile shear test specimen No. 2.

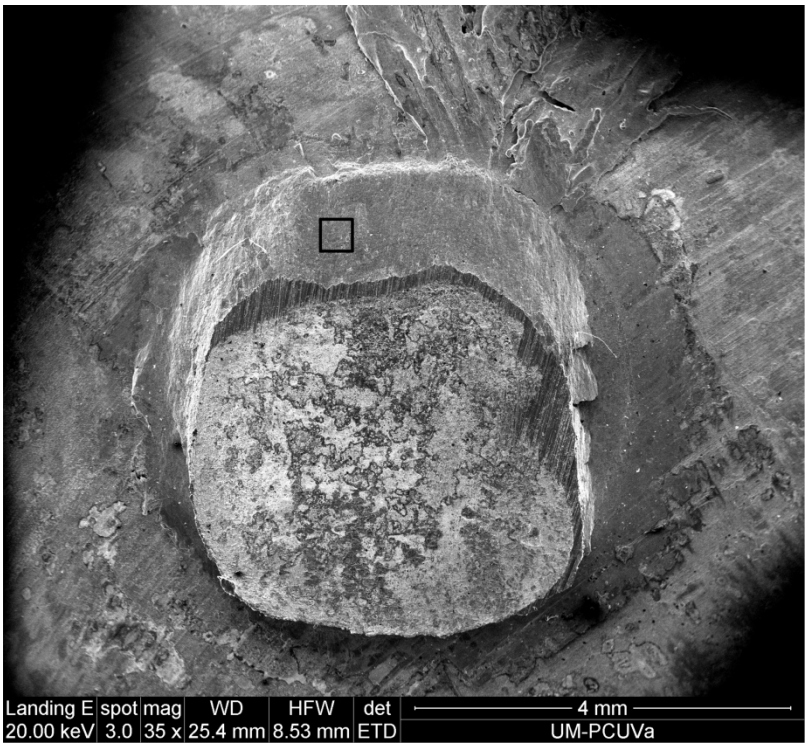


**Fig. 13.** SEM macrograph that shows the fracture of the tensile shear test specimen No. 2.

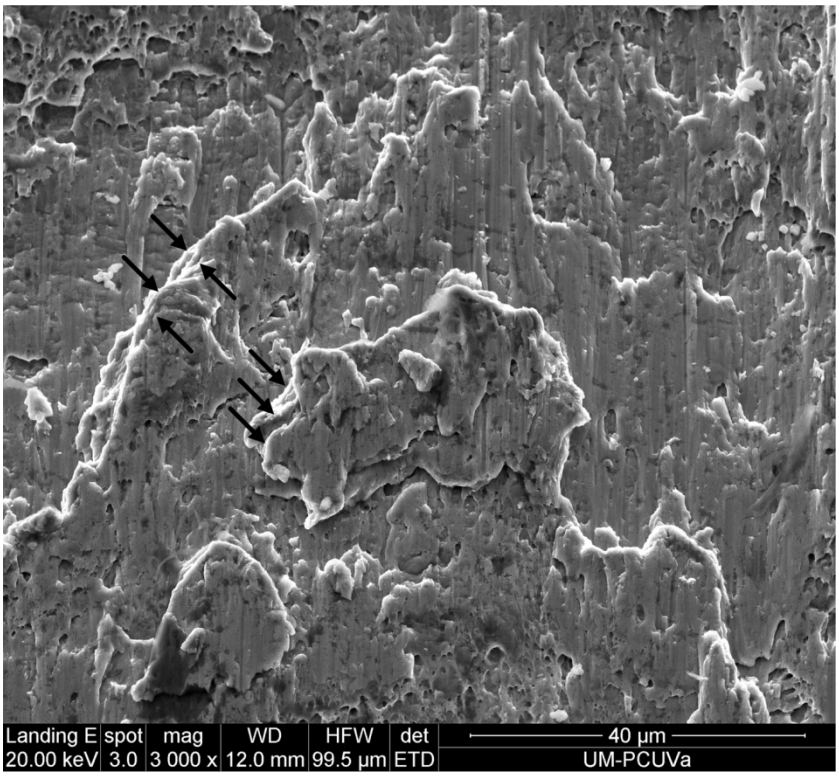


**Fig. 14.** SEM micrograph of the fracture surface of the tensile shear test specimen No. 2, obtained from the area indicated in the Fig. 13 in the flank side of the RSW joint [51]. The arrows show cleavage steps.

The analysis of the microstructure of specimen No. 5 (for an aging time of 100 h) confirms that, both in the weld nugget (Fig. 15) and in the base metal (Fig. 16), the presence of Widmanstätten η phase increases with aging time. In addition to this, and since there is no evidence of the presence of cellular η phase in the weld nugget for any aging time, it can be concluded that, at an aging temperature of 840 °C, in the weld nugget, the formation of Widmanstätten η phase inhibits the formation of cellular η phase.

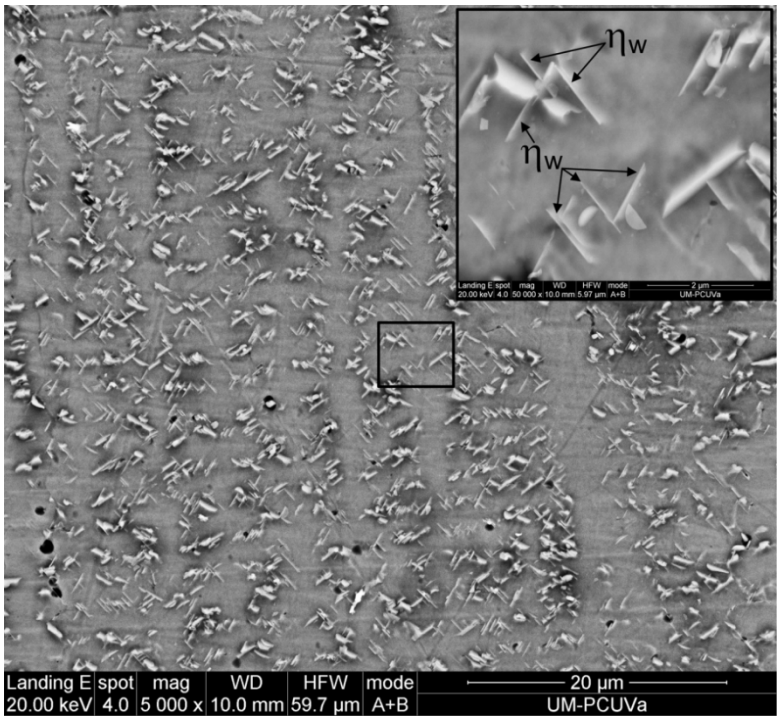


**Fig. 15.** SEM micrograph of the weld nugget of the tensile shear test specimen No. 5 where there is no evidence of the presence of γ' precipitates. There is an increase in the presence of Widmanstätten η phase in the weld nugget (compare with Fig. 9). The inset shows $\eta_w$ phase located at the interdendritic region. Electrolytic etching with etchant No. 83 according to ASTM E407-07 [31].

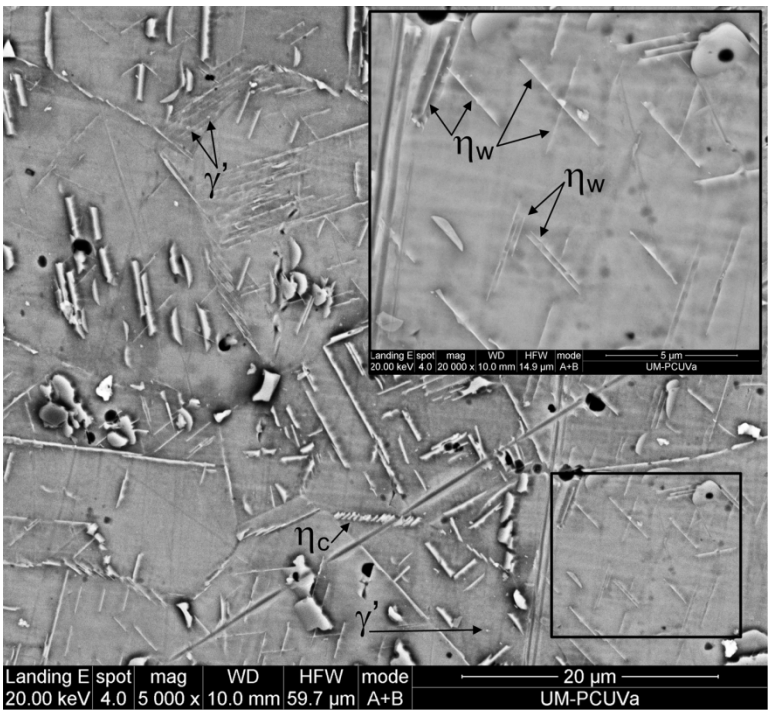


**Fig. 16.** SEM micrograph of the base metal of the tensile shear test specimen No. 5. The presence of Widmanstätten η ($\eta_w$) phase has increased whilst that of γ' precipitates has decreased so much that it is hardly noticeable. There is cellular η ($\eta_c$) phase at grain boundary. The inset shows $\eta_w$ phase into the grain. Electrolytic etching with etchant No. 83 according to ASTM E407-07 [31].

## 4 Conclusions

This work aims to study the effect of Widmanstätten η phase on TSS of RSW joints of A286 superalloy subjected to post-weld high temperature aging treatment. The major conclusions are:

1. The as-cast dendritic microstructure of the weld nugget and the austenite equiaxed-grain microstructure of the base metal have a different response to the post-weld high temperature aging treatment.
2. The Widmanstätten η plates are smaller but much more numerous in the weld nugget than in the base metal.
3. While in the base metal the Widmanstätten η phase precipitates into the grain, in the weld nugget precipitates at the interdendritic region because of the segregation of Ti towards the last-to-solidify interdendritic regions.
4. The presence of Widmanstätten η phase increases with aging time and, since it forms at the expense of γ' phase, the presence of γ' phase decreases.
5. From an aging time of 10 h, which is the is the aging time from which there is evidence of the presence of Widmanstätten η phase, the experimental values of TSS are even lower than that of the specimen that was subjected to no post-weld aging treatment.
6. Although the hardness increases with the presence of Widmanstätten η phase, the increase in hardness does not necessarily imply an increase in experimental TSS, and this fact can be attributed to the following causes: (i) the presence of Widmanstätten η phase may cause brittleness; (ii) the lower hardness of the zone around the weld nugget (which is also consistent with the pullout failure mode of the tensile shear test specimens); and (iii) the presence in the weld nugget of solidification cracks that occur during the last stages of solidification because of the inability of the nearly solidified weld metal to accommodate shrinkage stresses, and that are associated with the segregation of titanium and other solutes towards the last-to-solidify interdendritic regions that promotes the formation of a low melting point γ/Laves.
7. At an aging temperature of 840 °C, in the weld nugget, the formation of Widmanstätten η phase inhibits the formation of cellular η phase.

## Acknowledgements

The authors wish to thank Dr. Manuel Avella (Unidad de Microscopía del Parque Científico UVa) for the assistance with scanning electron microscopy.

## References


[1] S. Chen, H. Hu, M. Zhao, L. Rong, Effect of post-weld aging treatment on the precipitation and mechanical behavior of Fe-Ni based alloy weldment, Mater. Sci. Eng. A. 718 (2018) 363–370. doi:10.1016/j.msea.2018.01.127.

[2] L.K. Singhal, J.W. Martin, The mechanism of tensile yield in an age-hardened steel containing γ′ (ordered Ni3Ti) precipitates, Acta Metall. 16 (1968) 947–953. doi:10.1016/0001-6160(68)90061-8.

[3] A.W. Thompson, J.A. Brooks, The mechanism of precipitation strengthening in an iron-base superalloy, Acta Metall. 30 (1982) 2197–2203. doi:10.1016/0001-6160(82)90140-7.

[4] M.J. Zhao, Z.F. Guo, H. Liang, L.J. Rong, Effect of boron on the microstructure, mechanical properties and hydrogen performance in a modified A286, Mater. Sci. Eng. A. 527 (2010) 5844–5851. doi:10.1016/j.msea.2010.05.070.

[5] P. De Tiedra, Ó. Martín, M. San-Juan, Potentiodynamic study of the influence of gamma prime and eta phases on pitting corrosion of A286 superalloy, J. Alloys Compd. 673 (2016) 231–236. doi:10.1016/j.jallcom.2016.02.261.

[6] Ó. Martín, P. De Tiedra, M. San-Juan, Study of influence of gamma prime and eta phases on corrosion behaviour of A286 superalloy by using electrochemical potentiokinetic techniques, Mater. Des. 87 (2015) 266–271. doi:10.1016/j.matdes.2015.08.041.

[7] M. Seifollahi, S.H. Razavi, S. Kheirandish, S.M. Abbasi, The Mechanism of η Phase Precipitation in A286 Superalloy During Heat Treatment, J. Mater. Eng. Perform. 22 (2013) 3063–3069. doi:10.1007/s11665-013-0592-1.

[8] S. Asgari, Age-hardening behavior and phase identification in solution-treated AEREX 350 superalloy, Metall. Mater. Trans. A. 37 (2006) 2051–2057. doi:10.1007/BF02586125.

[9] X. Li, J. Zhang, L. Rong, Y. Li, Cellular η phase precipitation and its effect on the tensile properties in an Fe-Ni-Cr alloy, Mater. Sci. Eng. A. 488 (2008) 547–553. doi:10.1016/j.msea.2007.11.039.

[10] Z. Guo, H. Liang, M. Zhao, L. Rong, Effect of boron addition on hydrogen embrittlement sensitivity in Fe-Ni based alloys, Mater. Sci. Eng. A. 527 (2010) 6620–6625. doi:10.1016/j.msea.2010.06.073.

[11] A.W. Thompson, J.A. Brooks, Hydrogen performance of precipitation-strengthened stainless steels based on A-286, Metall. Trans. A. 6 (1975) 1431–1442. doi:10.1007/BF02641935.

[12] H. De Cicco, M.I. Luppo, L.M. Gribaudo, J. Ovejero-García, Microstructural development and creep behavior in A286 superalloy, Mater. Charact. 52 (2004) 85–92. doi:10.1016/j.matchar.2004.03.007.

[13] J.A. Brooks, A.W. Thompson, Microstructure and hydrogen effects on fracture in the alloy A-286, Metall. Trans. A. 24 (1993) 1983–1991. doi:10.1007/BF02666333.

[14] B.S. Rho, S.W. Nam, X. Xie, The effect of test temperature on the intergranular cracking of Nb-A286 alloy in low cycle fatigue, J. Mater. Sci. 37 (2002) 203–209. doi:10.1023/A:1013147319646.

[15] S. Chen, M. Zhao, L. Rong, Effect of Ti content on the microstructure and mechanical properties of electron beam welds in Fe-Ni based alloys, Mater. Sci. Eng. A. 571 (2013) 33–37. doi:10.1016/j.msea.2013.02.001.

[16] S.C. Ernst, W.A. Baeslack III, J.C. Lippold, Weldability of high-strength, low-expansion superalloys, Weld. J. 68 (1989) 418S–430S.

[17] ASM International Handbook Committee, Welding, in: J.R. Davies (Ed.), ASM Spec. Handbook. Stainl. Steels, ASM International, Materials Park, OH, 1994: pp. 340–401.

[18] J.A. Brooks, R.W. Krenzer, Progress toward a more weldable A-286, Weld. J. 53 (1974) 242S–245S.

[19] M.J. Cieslak, T.J. Headley, G.A. Knorovsky, A.D. Romig, T. Kollie, A comparison of the solidification behavior of INCOLOY 909 and INCONEL 718, Metall. Trans. A. 21 (1990) 479–488. doi:10.1007/BF02782428.

[20] R. Nakkalil, N.L. Richards, M.C. Chaturvedi, Microstructural characterization of INCOLOY 903 weldments, Metall. Trans. A. 24 (1993) 1169–1179. doi:10.1007/BF02657248.

[21] K. Shinozaki, Welding and joining Fe and Ni-base superalloys, Weld. Int. 15 (2001) 593–610. doi:10.1080/09507110109549411.

[22] G.S. Hoppin, R.E. Yount, Fusion Welding of Age-Hardenable Superalloys, SAE

Tech. Pap. 690102 (1969). doi:10.4271/690102.

[23] O. Martín, M. López, F. Martín, Redes neuronales artificiales para la predicción de la calidad en soldadura por resistencia por puntos, Rev. Metal. 42 (2006) 345–353. doi:10.3989/revmetalm.2006.v42.i5.32.

[24] Ó. Martín, P. De Tiedra, M. San-Juan, Combined effect of resistance spot welding and precipitation hardening on tensile shear load bearing capacity of A286 superalloy, Mater. Sci. Eng. A. 688 (2017) 309–314. doi:10.1016/j.msea.2017.02.015.

[25] S. Cissé, L. Laffont, M.-C. Lafont, B. Tanguy, E. Andrieu, Influence of localized plasticity on oxidation behaviour of austenitic stainless steels under primary water reactor, J. Nucl. Mater. 433 (2013) 319–328. doi:10.1016/j.jnucmat.2012.09.020.

[26] V. Ratna, D.S. Sarma, Influence of thermal fatigue on the microstructure of a Ni-base superalloy, Scr. Metall. Mater. 29 (1993) 467–472. doi:10.1016/0956-716X(93)90149-M.

[27] R.B. McCauley, M.P. Bennett, W.D. Bodary, G.C. Farrington, R.J. Gasser, W.W. Hurd, A.W. Schueler, T.W. Shearer, J.B. Silverberg, Resistance Spot Welding, in: T. Lyman (Ed.), Met. Handbook. Vol. 6 Weld. Brazing, 8th ed., American Society for Metals, Metals Park, OH, 1971: pp. 401–424.

[28] S. Aslanlar, The effect of nucleus size on mechanical properties in electrical resistance spot welding of sheets used in automotive industry, Mater. Des. 27 (2006) 125–131. doi:10.1016/j.matdes.2004.09.025.

[29] M. Safari, H. Mostaan, Experimental investigation of the effects of process parameters on the strength of eutectoid steel (AISI 1075) sheet resistance spot welds, Metall. Res. Technol. 113 (2016) 305. doi:10.1051/metal/2016005.

[30] O. Martín, P.D. Tiedra, M. López, M. San-Juan, C. García, F. Martín, Y. Blanco, Quality prediction of resistance spot welding joints of 304 austenitic stainless steel, Mater. Des. 30 (2009). doi:10.1016/j.matdes.2008.04.050.

[31] ASTM E407-07e1, Standard Practice for Microetching Metals and Alloys, 2007.

[32] Ó. Martín, V. Ahedo, J.I. Santos, P. De Tiedra, J.M. Galán, Quality assessment of resistance spot welding joints of AISI 304 stainless steel based on elastic nets, Mater. Sci. Eng. A. 676 (2016) 173–181. doi:10.1016/j.msea.2016.08.112.

[33] Ó. Martín, P. De Tiedra, M. López, M. San-Juan, C. García, F. Martín, Y. Blanco, Quality prediction of resistance spot welding joints of 304 austenitic stainless steel, Mater. Des. 30 (2009) 68–77. doi:10.1016/j.matdes.2008.04.050.

[34] P. Marashi, M. Pouranvari, S. Amirabdollahian, A. Abedi, M. Goodarzi, Microstructure and failure behavior of dissimilar resistance spot welds between low carbon galvanized and austenitic stainless steels, Mater. Sci. Eng. A. 480 (2008) 175–180. doi:10.1016/j.msea.2007.07.007.

[35] ISO 14273, Specimen dimensions and procedure for shear testing resistance spot, seam and embossed projection welds, 2000.

[36] J.P. Kong, T.K. Han, K.G. Chin, B.G. Park, C.Y. Kang, Effect of boron content and welding current on the mechanical properties of electrical resistance spot welds in complex-phase steels, Mater. Des. 54 (2014) 598–609. doi:10.1016/j.matdes.2013.08.098.

[37] A. Hasanbasoglu, R. Kacar, Resistance spot weldability of dissimilar materials (AISI 316L-DIN EN 10130-99 steels), Mater. Des. 28 (2007) 1794–1800. doi:10.1016/j.matdes.2006.05.013.

[38] Ó. Martín, M. Pereda, J.I. Santos, J.M. Galán, Assessment of resistance spot welding quality based on ultrasonic testing and tree-based techniques, J. Mater. Process. Technol. 214 (2014) 2478–2487. doi:10.1016/j.jmatprotec.2014.05.021.

[39] M. Zhou, H. Zhang, S.J. Hu, Relationships between quality and attributes of spot welds, Weld. J. 82 (2003) 72S–77S.

[40] J.M. Sawhill, J.C. Baker, Spot weldability of high-strength sheet steels, Weld. J. 59 (1980) 19S–30S.

[41] D.J. Radakovic, M. Tumuluru, Predicting Resistance Spot Weld Failure Modes in Shear Tension Tests of Advanced High-Strength Automotive Steels, Weld. J. 87 (2008) 96S–105S.

[42] ISO 6892-1, Metallic materials. Tensile testing. Part 1: Method of test at room temperature, 2009.

[43] V.A. Wills, D.G. McCartney, A comparative study of solidification features in nickel-base superalloys: microstructural evolution and microsegregation, Mater. Sci. Eng. A. 145 (1991) 223–232. doi:10.1016/0921-5093(91)90252-I.

[44] Z. Shi, J. Dong, M. Zhang, L. Zheng, Solidification characteristics and segregation behavior of Ni-based superalloy K418 for auto turbocharger turbine, J. Alloys Compd. 571 (2013) 168–177. doi:10.1016/j.jallcom.2013.03.241.

[45] K. Sivaprasad, S. Ganesh Sundara Raman, Influence of Weld Cooling Rate on Microstructure and Mechanical Properties of Alloy 718 Weldments, Metall. Mater. Trans. A. 39 (2008) 2115–2127. doi:10.1007/s11661-008-9553-y.

[46] W.L. Chuko, J.E. Gould, Development of Appropriate Resistance Spot Welding Practice for Transformation- Hardened Steels, Weld. J. 81 (2002) 1S–7S.

[47] Y. Yan, Y. Yan, Y. He, J. Li, Y. Su, L. Qiao, The mechanism of precipitation strengthening in Fe–Ni austenitic alloy electron beam weldment, Mater. Sci. Eng. A. 630 (2015) 85–89. doi:10.1016/j.msea.2015.02.014.

[48] S. Zhao, X. Xie, G.D. Smith, S.J. Patel, Research and Improvement on structure stability and corrosion resistance of nickel-base superalloy INCONEL alloy 740, Mater. Des. 27 (2006) 1120–1127. doi:10.1016/j.matdes.2005.03.015.

[49] E. Balikci, R.. Mirshams, A. Raman, Fracture behavior of superalloy IN738LC with various precipitate microstructures, Mater. Sci. Eng. A. 265 (1999) 50–62. doi:10.1016/S0921-5093(99)00012-X.

[50] P. De Tiedra, Ó. Martín, M. San-Juan, Effect of metallurgical evolution during post-weld aging treatment on localised corrosion of resistance spot welding joints of A286 superalloy, Corros. Eng. Sci. Technol. 53 (2018) 355–361. doi:10.1080/1478422X.2018.1473318.

[51] M. Tutar, H. Aydin, A. Bayram, Effect of Weld Current on the Microstructure and Mechanical Properties of a Resistance Spot-Welded TWIP Steel Sheet, Metals (Basel). 7 (2017) 519. doi:10.3390/met7120519.

Figure Captions

Figure 1. (A) Diagram (not to scale) that shows the location of the area where the micrograph (B) was taken from the tensile shear test specimen; (B) SEM micrograph of a cross sectioned tensile shear test specimen (not mechanically tested) where the arrows show solidification cracks in the weld nugget (WN); (C) SEM micrograph of the as-cast dendritic microstructure of the weld nugget. Electrolytic etching with etchant No. 83 according to ASTM E407-07 [31].

Figure 2. Load vs. displacement curve obtained from the tensile shear test performed on specimen No. 4. The TSS is shown on the curve.

Figure 3. Experimental (exp) TSS, which was obtained in the tensile shear test, and predicted (pred) TSS [39,40], of each of the seven tensile shear test specimens subjected to post-weld aging treatment. Specimen No. 0 was subjected to no post-weld aging treatment, i.e. it was in the solution treated (ST) condition and its aging time was considered as 0 h.

Figure 4. SEM micrograph of the weld nugget of the tensile shear test specimen No. 1. The γ' precipitates are located adjacent to the interdendritic region (IDR) whilst, as can be seen, there are γ' depleted zones in the dendrite core (DC). The inset provides the location of the studied zone. Electrolytic etching with etchant No. 83 according to ASTM E407-07 [31].

Figure 5. EDX spectrum obtained from the interdendritic region of the weld nugget of specimen No. 1.

Figure 6. SEM micrograph of the base metal of the tensile shear test specimen No. 1. The inset shows cellular η ($\eta_c$) phase at grain boundary. The γ' precipitates are not yet visible. Electrolytic etching with etchant No. 83 according to ASTM E407-07 [31].

Figure 7. SEM micrograph of the weld nugget of the tensile shear test specimen No. 2. The inset shows γ' precipitates and Widmanstätten η ($\eta_w$) phase located at the interdendritic region. The development of Widmanstätten η plates takes place along certain crystallographic directions [8]. Electrolytic etching with etchant No. 83 according to ASTM E407-07 [31].

Figure 8. SEM micrograph of the base metal of the tensile shear test specimen No. 2. The γ' precipitates are already visible, the Widmanstätten η ($\eta_w$) phase is formed into the grain and the cellular η ($\eta_c$) phase is also indicated. Electrolytic etching with etchant No. 83 according to ASTM E407-07 [31].

Figure 9. SEM micrograph of the weld nugget of the tensile shear test specimen No. 4 where there is no evidence of the presence of γ' precipitates. The inset shows Widmanstätten η ($\eta_w$) phase located at the interdendritic region. Electrolytic etching with etchant No. 83 according to ASTM E407-07 [31].

Figure 10. SEM micrograph of the base metal of the tensile shear test specimen No. 4. The presence of Widmanstätten η ($\eta_w$), which is heterogeneously distributed into the grains, is lower than in the weld nugget (where is homogeneously distributed along the interdendritic regions, see Fig. 9). There is cellular η ($\eta_c$) phase at grain boundary. The inset shows γ' precipitates and

Table Captions

Table 1. Chemical composition of A286 superalloy sheets (wt %).

Table 2. Tensile shear test specimens. Specimen No. 0 was subjected to no aging treatment, i.e. it was in the solution treated condition. Each of different aging treatments was followed by air cooling.

Table 3. Tensile test specimens (without welding). The specimen subjected to no aging treatment, was in the solution treated condition. Each of different aging treatments was followed by air cooling. The tensile strength ($\sigma_R$), obtained in the tensile test, is that of the base metal of the tensile shear test specimens indicated in Table 2.

Table 4. The predicted TSS values obtained from Eq. (1) and the experimental TSS values of the tensile shear test specimens indicated in Table 2 are shown.

Table 5. Chemical composition (wt%) of interdendritic region of the weld nugget of the specimen No. 1, determined by EDX and ratio k.